The Oxidation of Soot and Carbon Monoxide in Hydrocarbon Diffusion Flames

RAHUL PURI* and ROBERT J. SANTORO
Department of Mechanical Engineering, The Pennsylvania State University, University Park, PA 16802

and

KERMIT C. SMYTH
Building and Fire Research Laboratory, National Institute of Standards and Technology, Gaithersburg, MD 20899

Quantitative OH · concentrations and primary soot particle sizes have been determined in the soot oxidation regions of axisymmetric diffusion flames burning methane, methane/butane, and methane/1-butene in air at atmospheric pressure. The total carbon flow rate was held constant in these flames while the maximum amount of soot varied by a factor of seven along the centerline. Laser-induced fluorescence measurements of OH · were placed on an absolute basis by calibration against earlier absorption results. The primary size measurements of the soot particles were made using thermophoretic sampling and transmission electron microscopy. OH · concentrations are greatly reduced in the presence of soot particles. Whereas large super-equilibrium ratios are observed in the high-temperature reaction zones in the absence of soot, the OH · concentrations approach equilibrium values when the soot loading is high. The diminished OH · concentrations are found to arise from reactions with the soot particles and only to a minor degree from lower temperatures due to soot radiation losses. Analysis of the soot oxidation rates computed from the primary particle size profiles as a function of time along the flame centerlines shows that OH · is the dominant oxidizer of soot, with O_2 making only a small contribution. Higher collision efficiencies of OH · reactions with soot particles are found for the flames containing larger soot concentrations at lower temperatures. A comparison of the soot and CO oxidation rates shows that although CO is inherently more reactive than soot, the soot successfully competes with CO for OH · and hence suppresses CO oxidation for large soot concentrations.

I. INTRODUCTION

In recent years increasing attention has been devoted to oxidation processes in hydrocarbon diffusion flames due to their key role in the production of combustion-generated pollutants. Not only does the soot oxidation step determine the amount of smoke that will be emitted from a flame, but it also strongly influences the quantity of carbon monoxide (CO) that will survive a given combustion process [1]. Emissions of both CO and soot particles present significant fire hazards, indicate poor combustion efficiency, and are objectionable from an environmental standpoint.

Prior to the work of Fenimore and Jones [2] that elucidated the importance of OH · radicals, soot oxidation rates were calculated using the expression determined by Nagle and Strickland-Constable (NSC) for pyrographite oxidation [3] by assuming that molecular oxygen alone was responsible. Neoh et al. [4] also showed that OH · is the primary oxidant of soot in the main reaction zone of premixed flames and that the contribution of molecular oxygen is significant only when the oxygen mole fraction is greater than 5%. The recent study of Dixon-Lewis et al. [5] has reopened the question of whether OH · or O_2 is the primary oxidant of soot in premixed flames. They proposed a catalytic mechanism in which H atoms react with O_2 at or close to the soot surface to produce either OH · radicals or O atoms, which then more efficiently attack soot.

Soot oxidation studies have often assumed that soot particles are spherical and have used laser light scattering and extinction measurements to obtain information on their size [6].

* Current address: Allison Engine Company, P. O. Box 420, Speed Code T-14, Indianapolis, IN 46206-0420.

Published by Elsevier Science Inc.

0010-2180/94/$7.00

In reality, the soot particles are agglomerates of a variable number of smaller, uniformly sized, approximately spherical "primary" particles [7]. Therefore, the assumption of spherical particles can result in a significant error in the estimation of the particle surface area and thus the oxidation rate. With the incorporation of fractal concepts, it is now possible to obtain a reasonable estimate of the surface area of agglomerated soot particles [8].

Despite these advances in characterizing the soot particle surface area, complexities exist in determining the fraction of the surface area that participates in reactions, that is, the number of active sites. Although the concept of reactions at active sites is relatively new in the area of soot surface growth, it was proposed over 30 years ago to explain the heterogeneous reactions of various gases with carbon [9]. In fact the NSC expression is based on a concept similar to the active sites approach. Howard [10] has recently suggested an active site description involving radicals for soot oxidation by OH · . His reevaluation of previous data [4] shows an interesting correlation between the H/C ratio in the soot and the measured collision efficiency of soot with OH · .

Not much is known about the nature and origin of active sites for either soot growth or oxidation processes. Tesner [11] argues that active sites are formed when reactive species collide with the incipient particle surface. Once formed, these sites are thought to be self-renewing [12] and are not affected by coagulation, surface growth, or gas-phase chemistry [13]. It is not known whether the same active sites that participate in the surface growth reactions following soot inception also play a role in oxidation processes. Recent x-ray photoelectron spectroscopy investigations [14, 15] have shown adsorbed as well as chemically bound oxygen to be present on soot particles.. It has been suggested that the active sites include surface-adsorbed oxygenated complexes that are responsible for the catalytic reactivity of the carbon particles [15].

Our understanding of soot oxidation in terms of both the reactive area as well as the primary oxidant is still not complete. In the present investigation concentration profiles of the hydroxyl radical have been obtained in the soot oxidation regions of laminar, hydrocarbon diffusion flames using laser-induced fluorescence. The data have been placed on a quantitative basis by calibrating [16] against an earlier absorption measurement. Soot primary particle size measurements have also been made using a thermophoretic sampling procedure [7] followed by transmission electron microscopy (TEM). The time evolution of the primary particle profiles is used in conjunction with results of a fractal aggregate analysis to calculate soot oxidation rates. Specific attention is devoted here to the factors that control the OH · concentrations in the soot oxidation region.

II. EXPERIMENTAL APPROACH

A coannular burner consisting of a 1.1-cm-diameter fuel tube and a concentric 10.2-cm-diameter air annulus [17] was used to establish the laminar diffusion flames. CP grade purity (99%) fuels were used in these studies, while an in-house compressor was employed to supply the air. The air and fuel flows to the burners were metered with rotameters, which were arranged to allow mixing of two fuels. A fuel mixture approach was adopted in order to vary the soot concentration while keeping the total carbon flow rate constant, which ensured similar flame sizes and shapes. Flames burning methane (9.8 cm^3/s) and methane (5.6 cm^3/s) doped with either butane (1.05 cm^3/s) or 1-butene (1.05 cm^3/s) were studied. The air flow rate was maintained at 1300 cm^3/s for all flames.

A. OH · Concentration Measurement

Figure 1 presents a schematic diagram of the laser-induced fluorescence measurement setup. The UV beam was produced by frequency doubling the output of a Nd:YAG pumped dye laser. The wavelength was tuned to 283.55 nm, which corresponds to the excitation of the $Q_1(8)$ line of the $A^2\Sigma^+ \leftarrow X^2\Pi_i$ (1, 0) band of OH · . Excitation from the $N'' = 8$ level minimizes the Boltzmann population correction with temperature (less than 5% over the temperature range 1400–2100 K). Since the pulse energy was high enough (~ 1 mJ/pulse) to easily saturate this strong transition, only the reflected

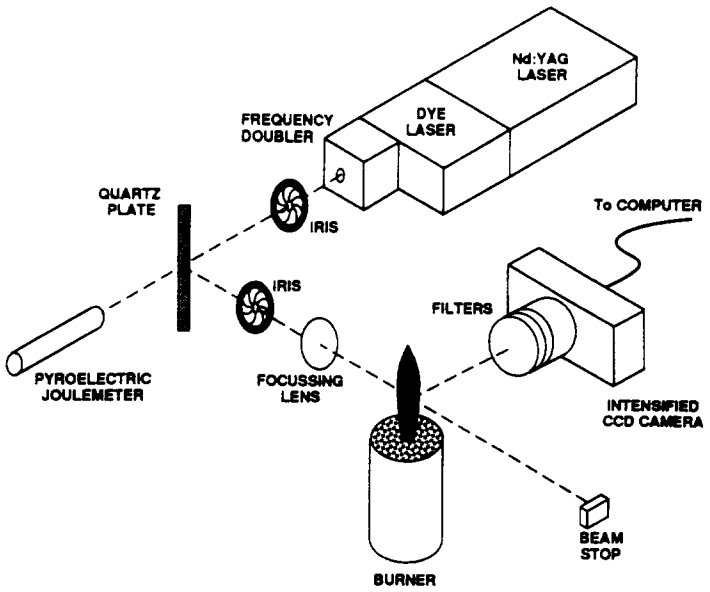

Fig. 1. Schematic diagram of the laser-induced fluorescence experimental setup.

beam from the first surface of a thick piece of quartz ($\sim$ 0.03 mJ/pulse) was passed through the flame. This procedure ensured that the laser-induced fluorescence signals were linear with the laser energy. A pyroelectric joulemeter was placed behind the quartz plate to monitor the laser energy for each pulse. The fluorescence signal was collected at 90° with a cooled CCD (charge coupled device) camera equipped with a microchannel plate image intensifier. Glass filters placed in front of the camera attenuated elastically scattered light from the soot particles and transmitted the (0, 0) and (1, 1) emission bands of OH·, as well as the broadband fluorescence which has been attributed to polycyclic aromatic hydrocarbons [18].

The details of the experimental procedure have been described elsewhere [16] and are only briefly outlined here. At each measurement location two one-dimensional images were obtained with the laser wavelength tuned on and off the $Q_1(8)$ excitation line of OH·. Relative intensity radial profiles were obtained from these images by binning data over several pixel rows in the region of interest. While the on-resonance profiles show signals due to OH· fluorescence, light scattered by soot particles, and PAH fluorescence, the off-resonance profiles exhibit only the latter two contributions. Since the off-resonance images were obtained by tuning the laser wavelength by only 0.03 nm, the signals due to light scattered by soot particles and broadband PAH fluorescence were unchanged. Thus, subtracting the off-resonance profile from the on-resonance profile gives the raw OH· signal even in regions where there are significant amounts of soot.

The relative intensity of the OH· signal was calibrated using an earlier absorption measurement in a methane/air diffusion flame on a Wolfhard-Parker burner [19]. Detailed measurements of the major species have been obtained along the centerline for the axisymmetric flames studied here [1], and these allow a complete quenching correction to be made [19–21]. For the radial OH· profiles only an approximate correction for the overall quenching rate (proportional to $1/\sqrt{T}$) was applied [16], since radial species profile data are not available in these flames. An additional correction must be made for determining the OH· concentrations along the centerline in order to account for the attenuation of the laser beam intensity by soot particles (absorption by OH· is less than 1% [16]). This attenuation leads to asymmetric fluorescence profiles, with the asymmetry being greatest for the methane/1-butene flame which contains the largest soot concentrations. The OH· signal profiles have

been corrected using local extinction measurements of the soot particle field in identical flames [22]. Extinction values depend upon the wavelength of light being used and the refractive index of the soot particles at that wavelength. Since the latter quantity has not be obtained with certainty, the extinction profile measurements [22] were scaled such that symmetric OH · fluorescence profiles resulted. The intensity of the laser beam could then be derived at each radial flame location.

B. Soot Primary Particle Size Measurements

A thermophoretic sampling technique similar to that used by Dobbins and Megaridis [7] was employed to measure the size of the primary soot particles. The thermophoretic probe consisted of a carbon-coated 200-mesh copper grid held in place between two strips of sheet metal, machined to expose the grid to the flame. The probe was rapidly inserted into the flame environment ($\sim$ 3.3 m/s) for a brief exposure duration of 50 ms before being quickly withdrawn. This exposure time is short enough to provide a cold surface to collect soot particles by thermophoresis as well as to quench any heterogeneous reactions on the captured particles [7]. The rapid insertion and retraction motion was made possible by mounting the probe on the displacement rod of a double acting pneumatic cylinder. The direction reversal of this cylinder was achieved by supplying the driving air (at 40 psi) through a three-way solenoid valve controlled with a variable time-delay relay circuit.

Transmission electron microscopy (TEM) was used to examine the grids, and micrographs were obtained at a magnification of 60,000. These micrographs were then imaged with a CID (charge injection device) camera that provided an additional, approximately ten-fold magnification. The CID camera software was utilized to measure the primary particle size, d_p, by locating the measurement cursor at diametrically opposite sides of each spherical primary particle and noting the coordinates. A minimum of 75 d_p measurements were made at each flame location. An image of engineering graph paper was also obtained to provide an absolute length calibration for the CID camera magnification. Finally, the primary particle sizes were obtained by accounting for the TEM magnification. The camera images had a pixel resolution varying from 0.6 nm for the methane flame images to 1.0 nm for the methane/1-butene flame images.

III. RESULTS

A. OH · Concentration Measurements

Figure 2 presents the OH · concentration profiles in the 9.8-cm^3/s methane/air diffusion flame at several axial locations above the fuel tube exit. The methane flame has a visible height of 10.7 cm, corresponding to the location where soot particles are completely oxidized. Therefore, the OH · concentration profiles at 10.2 and 11.4 cm correspond to locations immediately below and above the visible flame tip, respectively. It is interesting that the profile at 10.2 cm shows two OH · maxima and a valley in the region where the soot particles are being oxidized. In contrast, diffusion processes at this height result in maxima along the centerline for all fuel-derived major species (such as CO_2, CO, and H_2O) as well as for the temperature. Once the soot particles are completely oxidized, the OH · concentration profile shows a single peak along the flame centerline at an axial position of 11.4 cm.

Figure 3 presents the OH · concentration results in the methane/butane flame. As in the methane flame, the OH · profiles show evidence of OH · consumption close to the flame tip. In the methane/butane flame the profiles at 11.4 and 12.7 cm correspond to locations immediately below and above the visible flame tip at 11.7 cm. Although diffusion processes result in a single maximum at the centerline for the temperature and the fuel-derived major species, the OH · concentration profile again exhibits two maxima at the axial location of 11.4 cm. Above the visible flame tip where there are no soot particles, the OH · profile shows a single peak along the centerline.

Figure 4 presents the OH · concentration results in the methane/1-butene flame. The methane/1-butene flame does not have a visi-

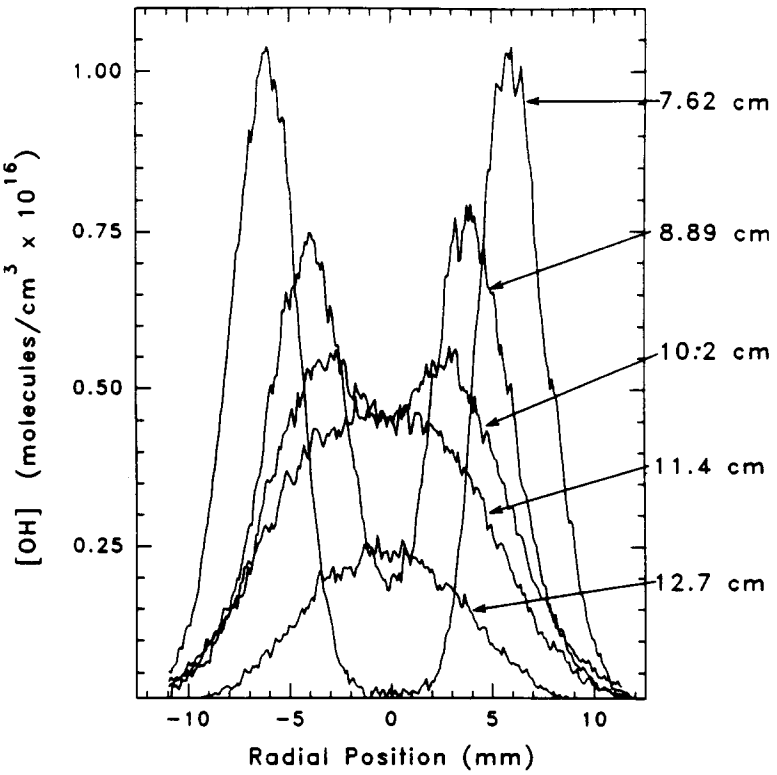

Fig. 2. OH · concentration profiles in the pure methane diffusion flame at axial positions of 7.6, 8.9, 10.2, 11.4, and 12.7 cm from the fuel tube exit.

ble flame tip, since it emits smoke. In this respect the lack of buildup of OH · along the centerline of this flame suggests that reactions between OH · and soot particles strongly reduce the OH · concentrations.

B. Soot Primary Particle Size Measurements

Figure 5 presents the volume mean diameter, d_{p30}, as a function of time along the centerline of the methane, methane/butane, and methane/1-butene flames. The values of d_{p30} were determined from the d_p measurements by taking the cube root of the averaged value of d_p^3. Also shown in Fig. 5 are the soot volume fraction measurements, f_v [22]. Velocity data obtained from laser velocimetry measurements in identical flames [22] were used to convert the axial positions to time. The primary particle size in the methane and the methane/butane flames decreases rapidly and shows a convex upwards shape, consistent with particle burnout. In contrast, the methane/1-butene flame shows a concave upward shape, and the particle sizes approach a constant value. This behavior is consistent with smoking conditions.

The soot volume fraction measurements shown in Fig. 5 are related to the volume mean diameter through the number concentration of the primary particles N_p:

$$f_v = \frac{\pi}{6} d_{p_{30}}{}^3 N_p. \tag{1}$$

In the present analysis N_p is assumed to be constant along the flame centerline. This assumption is based on (1) the results of a fractal aggregate analysis [8] applied to a laminar ethene/air diffusion flame along a nearly isothermal streamline passing through the location of the maximum soot volume fraction [23], (2) the small temperature variation (less than 250 K) observed in the soot oxidation region of the flames studied here, and (3) the narrow size distribution of the primary particle size at each measurement location.

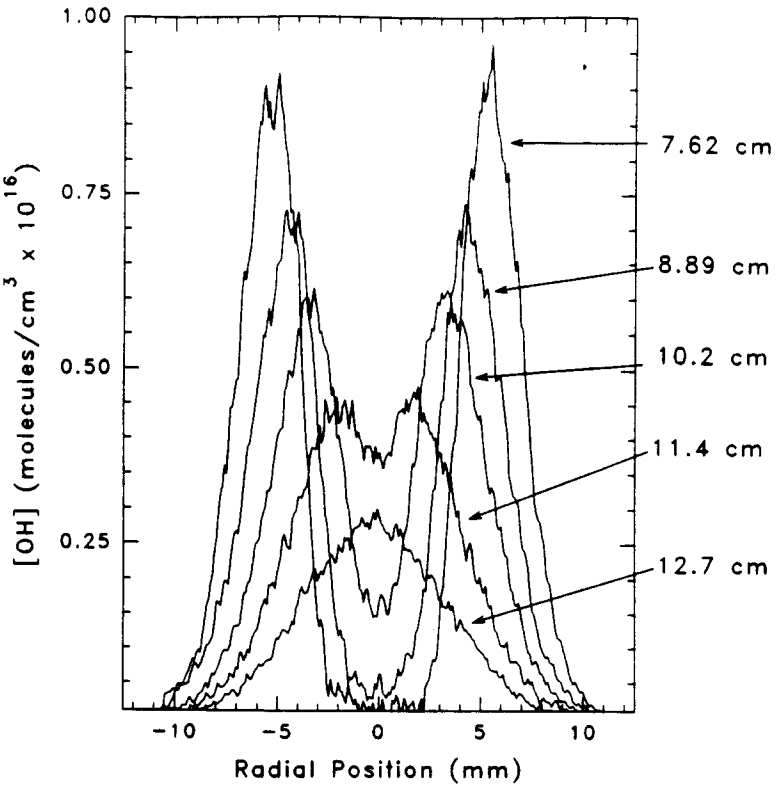

Fig. 3. OH · concentration profiles in the methane/butane diffusion flame at axial positions of 7.6, 8.9, 10.2, 11.4, and 12.7 cm from the fuel tube exit.

Assuming that there is no slip between the particles and the hot combustion gases, a ±125 K temperature variation at 1500 K will cause the number concentration of primary particles to change by less than ±10% (as determined from the temperatures and the ideal gas law). The radial temperature profiles in the oxidation region of the flames studied exhibit temperature gradients less than 66 K/mm near the centerline. An effective upper limit of the lateral thermophoretic displacement of soot particles, as they traverse the region studied, is estimated to be only 0.08 mm. Due to their large mass, transport of soot particles by diffusion is negligible.

The size distribution of the primary particles at each measurement location in this study is narrow (±18%), suggesting that each primary particle at a given location in the flame grows and oxidizes at roughly the same rate. Therefore, the assumption of a constant primary particle number concentration N_p should hold for our conditions.

Data in the methane/butane flame support the relative constancy of N_p, which has also been reported by others along convective streamlines in premixed propane/oxygen [24] and ethene/air laminar diffusion [25] flames. In the methane flame there are insufficient soot volume fraction data for a similar check. For this flame the soot volume fraction, f_v, and the d_{p30} results overlap in time only near 0.115 s (Fig. 5). Here the shape of the profiles, i.e., the small rate of change with respect to time, suggests that both f_v and d_{p30} are close to their maximum values along the centerline. For the methane/1-butene flame the measurements indicate a significant increase in N_p, particularly at earlier times where the soot volume fraction increases, whereas the primary particle size decreases. However, this may be an artifact of the thermophoretic sampling procedure because the annular soot volume fraction in the methane/1-butene flame is more than a factor of two higher than the centerline values at the earlier times examined

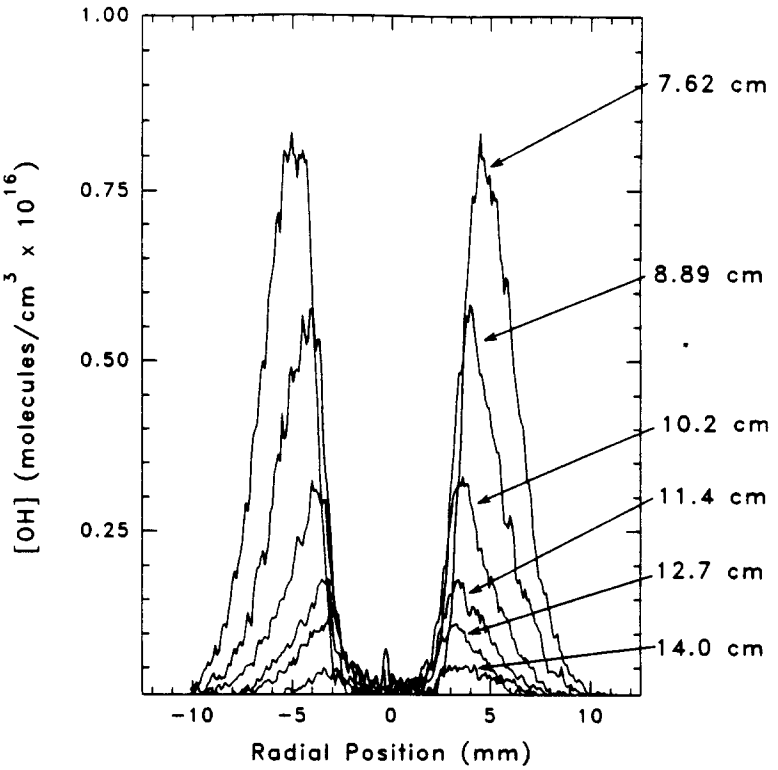

Fig. 4. OH · concentration profiles in the methane/1-butene diffusion flame at axial positions of 7.6, 8.9, 10.2, 11.4, 12.7, and 14.0 cm from the fuel tube exit.

in the soot oxidation region. Thus, the centerline TEM samples may have been contaminated with soot particles from the annular region which contains larger primary particles. Of the flames studied here such a situation occurs in the oxidation region only for the methane/1-butene flame. In the methane and methane/butane flames, the soot volume fraction peaks at the centerline for the axial positions examined in the oxidation region. At radial locations corresponding to the rapidly oxidizing annular soot region, the soot volume fraction is lower than the centerline values by up to a factor of seven. This discussion is relevant when considering the collision efficiency of OH · with soot (see section IV.D).

IV. DISCUSSION

The OH · measurements in the methane, methane/butane, and methane/1-butene flames show that the OH · concentration is suppressed in the presence of soot particles. The larger the soot concentration, the greater the effect upon the OH · levels due to its apparent consumption in the soot oxidation region. Thus, soot particles are likely to reduce the amount of OH · available for CO oxidation. Prior investigations have also shown that the yield of CO from hydrocarbon diffusion flames is closely related to the measured soot concentrations within the flame, with larger CO concentrations surviving at the higher soot loadings [1, 26]. For the flames of the present study the CO concentration measurements have been made primarily along the centerline [1]. Thus, attention will be focused on centerline measurements in the oxidation region.

A. Superequilibrium OH · Concentrations

Figure 6 shows the OH · concentration results along the centerline as a function of the axial position above the fuel tube exit. The error bars represent the standard error of the 22 pixel measurements that constitute the approx-

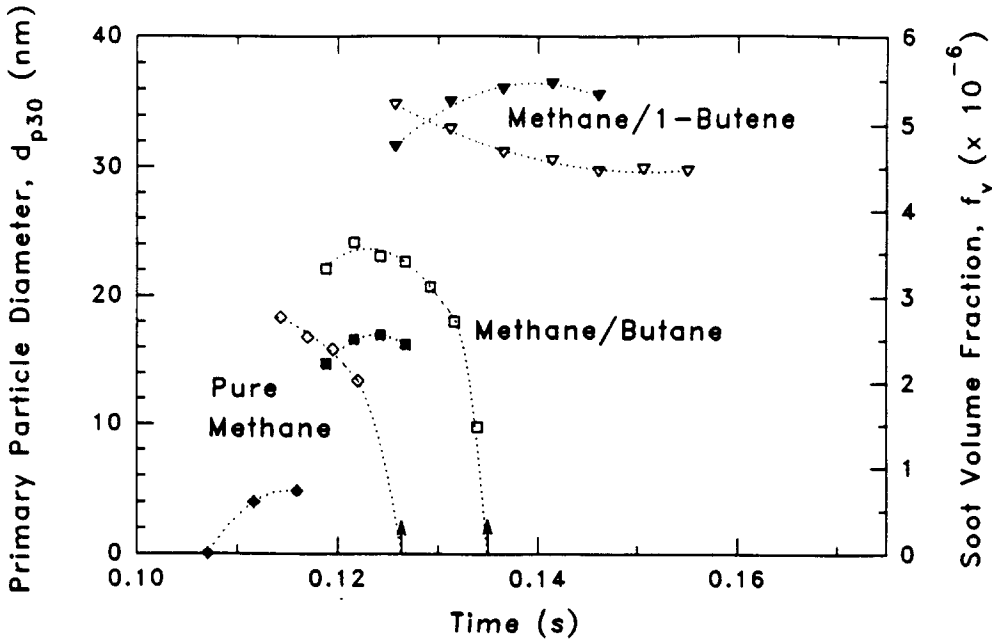

Fig. 5. Comparison of the soot volume fraction, f_v (solid symbols), and the primary particle volume mean diameter, $d_{p_{30}}$ (open symbols), as a function of time along the centerline in the three flames. The data for $d_{p_{30}}$ correspond to axial centerline positions of 7.6–9.5 cm in the pure methane flame (◇, ◆); 7.6–11.4 cm in the methane/butane flame (□, ■); and 7.6–15.2 cm in the methane/1-butene flame (▽, ▼). The arrows on the time axis denote the visible flame tip locations of the methane and the methane/butane flames.

imately constant signal about the centerline (±1 mm). These statistical uncertainties are smaller than the symbol size for the methane and methane/butane flames where the OH · concentrations are high and the signal-to-noise ratios are large. Also presented in Fig. 6 are the centerline measurements of temperature, soot volume fraction, and CO for the three flames of this study.

Figures 2–4 and 6 clearly show that as the soot concentration increases (going from the methane to the methane/butane to the methane/1-butene flame), the centerline OH · concentration decreases. The peak centerline soot volume fractions are 0.76, 2.6, and 5.5 ppm in the methane, the methane/butane, and the methane/1-butene flames, respectively [22]. A noteworthy feature of Fig. 6 is that the OH · concentrations in the methane and the methane/butane flames reach approximately the same value along the centerline once the soot particles are completely oxidized. At an axial location of 12.7 cm the centerline temperatures (1610 K and 1549 K) and the local stoichiometries (0.84 and 0.86) are also closely similar in these two flames (see also Table 1).

The centerline and peak OH · concentration data have also been compared with equilibrium predictions [27]. These results are of particular interest to investigators modeling the soot oxidaton process [28–31] since radical concentrations thus far have been either estimated from equilibrium considerations or assumed. Here, the equilibrium OH · values were calculated using the measured temperatures and the local equivalence ratio obtained from the species concentration measurements [1]. Table 1 presents the results along with the local flame conditions (T and ϕ) at each measurement location. With increasing height and decreasing ϕ, the superequilibrium OH · levels decrease along the centerline for all flames. It is interesting to note in the methane/1-butene flame that emits smoke the OH · concentration along the centerline quickly approaches the equilibrium prediction at the higher measurement locations where $\phi < 1$. For axial loca-

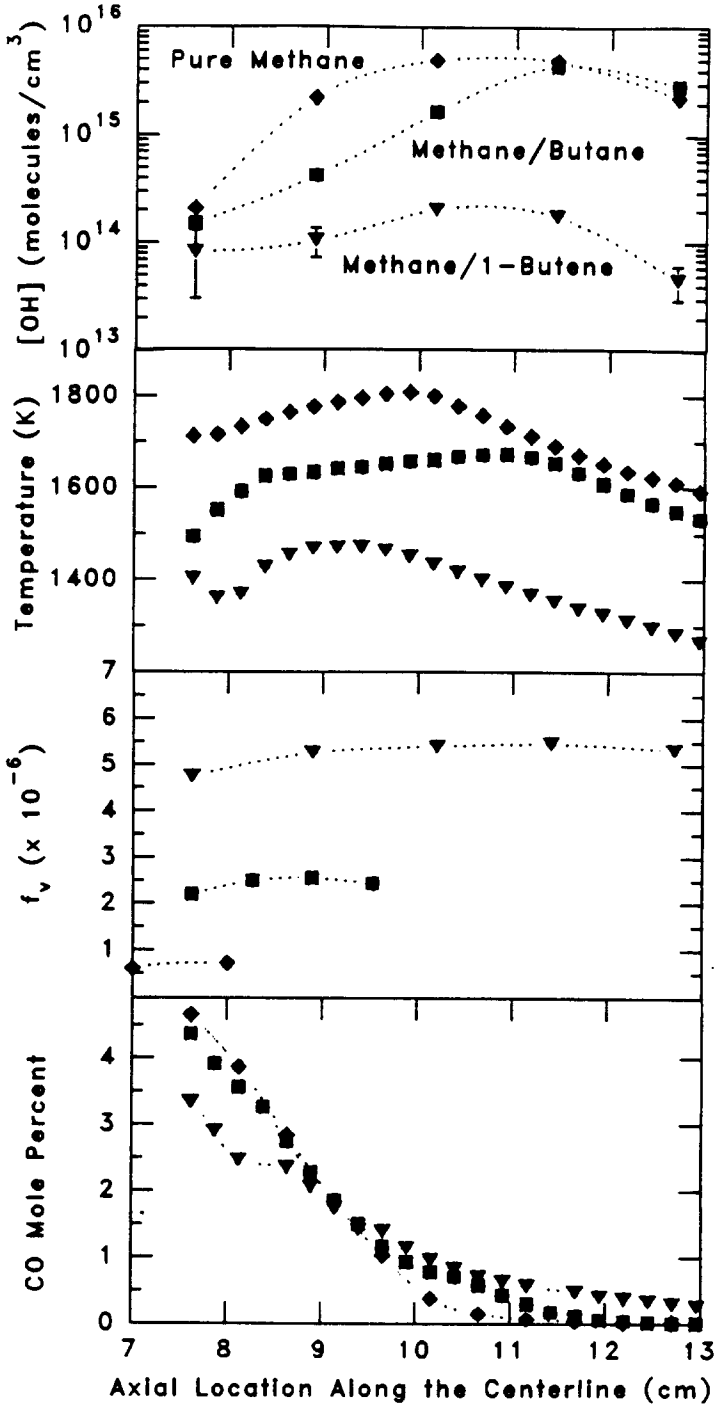

Fig. 6. Centerline OH · concentration profiles in the three flames; the error bars denote statistical uncertainties only (see text). Also shown are the radiation corrected thermocouple temperature, soot volume fracton, and CO measurements. The symbols for the methane (◆), methane/butane (■), and methane/1-butene (▼) flames are the same for each panel.

TABLE 1

Summary of Flame Measurements Obtained Along the Centerline and at the Location of the Peak OH · Concentration for Various Heights H (cm) Above the Fuel Tube Exit[a]

	Centerline					Location of Peak OH ·		
Flame	H	ϕ	T	$[OH\cdot]_{Ex}$	SR	T	$[OH\cdot]_{Ex}$	SR
CH_4	7.62	1.21	1712	2.1E14	5.5	1748	1.0E16	6.2
	8.89	1.06	1774	2.2E15	14	1799	7.9E15	3.6
	10.2	0.99	1798	5.0E15	4.1	1742	5.7E15	3.6
	11.4	0.92	1690	4.9E15	4.8	1690	4.9E15	4.7
	12.7	0.84	1610	2.3E15	3.3	1610	2.3E15	3.3
CH_4/C_4H_{10}	7.62	1.19	1494	1.5E14	69	1718	9.3E15	6.9
	8.89	1.06	1634	4.3E14	15	1658	7.4E15	8.0
	10.2	1.01	1660	1.6E15	16	1611	6.1E15	9.1
	11.4	0.96	1653	4.4E15	6.6	1610	4.7E15	7.1
	12.7	0.86	1549	2.8E15	6.6	1549	2.8E15	6.7
$CH_4/1\text{-}C_4H_8$	7.62	1.16	1403	8.2E13	154	1560	8.0E15	17.4
	8.89	1.06	1469	1.0E14	37	1444	5.8E15	32.2
	10.2	0.99	1435	2.0E14	2.2	1377	3.2E15	32.2
	11.4	0.93	1352	1.8E14	2.7	1293	1.8E15	43.0
	12.7	0.85	1283	4.6E13	1.2	1242	1.1E15	48.9
	14.0	0.77	1236	2.7E12	0.1	1192	5.3E14	42.2

[a] The OH · number densities (molecules/cm^3), local stoichiometries ϕ, temperatures T (K), and superequilibrium OH · concentration ratios (SR) are shown. For the peak OH · results, a local stoichiometry of $\phi = 0.85$ has been assumed [16].

tions where the peak OH · concentrations occur in the annular region, greater departures from the equilibrium predictions, calculated at an assumed stoichiometry of $\phi = 0.85$ [16], are observed as the soot concentration increases (see Table 1). The same qualitative result has been observed for the maximum OH · concentrations measured in a series of ethene/air diffusion flames in which the soot volume fraction was varied [16].

Table 1 shows that while the peak OH · concentration in the methane/1-butene flame exhibits larger superequilibrium values, the centerline OH · concentrations are closer to equilibrium values for $\phi < 1$ than in the other flames of this study. This result can be rationalized as follows. As the soot concentration increases in a hydrocarbon diffusion flame, the temperatures decrease due to heat loss by radiation. Apparently, the concentrations of the major radicals (OH · , O:, and H ·), which are controlled by fast, bimolecular shuffle reactions and three-body recombination reactions, do not adjust quickly to the lower temperatures. Thus, with increasing soot concentrations and lower flame temperatures, larger superequilibrium OH · concentrations are observed at the location of peak OH · concentration. Note that there are no soot partcles in this region. Within the envelope of the visible flame the lower superequilibrium ratios can be ascribed to the presence of soot particles. The large soot surface area can serve as a sink for the radical pool in two ways: as a reactive partner and/or as a chaperon, M, for the three-body recombination reactions.

Carbon has been reported by Mulcahy and Young [32] to efficiently catalyze the recombination reaction of OH · with H atom at 298 K. These workers report a lower limit of 0.04 for the collision efficiency between OH · and soot, $\eta_{OH,c}$, for the catalyzed recombination reaction:

$$H\cdot + OH\cdot + C \rightarrow H_2O + C.$$

This reaction was assumed to be first order in the OH · concentration and zero order in the H-atom concentration [32]. If we assume the same value of the collision efficiency for our conditions, the normalized reaction rate of OH · (determined from $\omega_{OH}/[OH\cdot]$) is 17,510 s^{-1} in the methane/1-butene flame at

the centerline for an axial position of 8.89 cm; the temperature is 1469 K. At the same location $\omega_{OH}/[OH\cdot]$ for the termolecular recombination reaction in the gas phase

$$H\cdot + OH\cdot + M \rightarrow H_2O + M$$

is calculated to be only 9 s^{-1}. Here the H-atom concentration was obtained from the OH·, H_2, and H_2O concentration measurements by assuming equilibration of:

$$H\cdot + H_2O \leftrightarrows OH\cdot + H_2.$$

Appropriate rate constants were obtained from the work of Baulch et al. [33]. This analysis indicates that the presence of soot particles reduces the local OH· concentration and can cause a more rapid adjustment of superequilibrium OH· levels toward equilibrium values.

B. Thermal versus Chemical Effects on the OH· Concentration

Consideration will now be given to the factors that affect the OH· concentrations in these flames. Figures 2–4 and 6 show a strong dependence of the OH· concentration upon the local soot concentration. From equilibrium calculations one finds that the OH· concentration depends on both the temperature and on the local stoichiometry, ϕ. It is also possible that the amount of CO, which is not uniquely related to ϕ [1], will affect the OH· concentration. Therefore, the OH· concentration can be functionally represented as follows:

$$[OH\cdot] = f(\phi, T, [\text{Soot}], [\text{CO}]). \quad (2)$$

The relative contributions of thermal versus chemical effects on the OH· concentration are difficult to establish in flames, where the controlling parameters are highly coupled. For example, as the soot concentration increases, the temperature decreases due to radiative heat transfer. Hydrocarbon diffusion flames, therefore, do not offer the opportunity of holding one parameter fixed and varying the others. However, estimates of thermal versus chemical effects can still be made. Equilibrium predictions of the OH· concentration show a weak dependence on ϕ in the fuel lean region ($\phi \leq 0.95$). Therefore, Eq. 2 can be rewritten as

$$[OH\cdot] = f(T, [\text{Soot}], [\text{CO}]) \quad (3)$$

for $\phi \leq 0.95$. The OH· concentration as a function of the temperature alone can be established at the locations of the maximum OH· concentration and at greater radial locations where $\phi \leq 0.85$. Here there are no soot particles present, and the CO concentration is either very low or undetectable (< 100 ppm). Figure 7 plots the temperature dependence of the OH· concentration in the methane/butane and the methane/1-butene flames. The steep gradients in both the OH· concentration and the temperature measurements require careful alignment of their respective profiles for this analysis. The values of the OH· concentrations presented in Fig. 7 are averages of up to five measurements at the same temperature but for different radial profiles. The uncertainties in the OH· concentrations are estimated to be as much as ±50% from the scatter of the values about their mean.

There are two major mechanisms which control OH· concentrations in the oxidation region of hydrocarbon diffusion flames, namely thermal quenching due to radiation losses (thermal effect) and reactions of OH· with soot particles and CO (chemical effect). These can be examined by comparing the $[OH\cdot] = f(T)$ data from Fig. 7 with $[OH\cdot] = f(T, [\text{Soot}], [\text{CO}])$ for $\phi \leq 0.95$ obtained from the centerline profiles shown in Fig. 6. The methane/ butane and the methane/1-butene flames have been selected for this analysis since the measured values of the local stoichiometry as a function of the axial location are closely similar in these flames. If

$$F_1 = \frac{f_1(T)}{f_2(T)} \quad \text{and} \quad F_2 = \frac{f_1(T, [\text{Soot}], [\text{CO}])}{f_2(T, [\text{Soot}], [\text{CO}])}, \quad (4)$$

where the subscripts 1 and 2 represent the flames methane/butane and methane/1-butene, respectively, then the relative contribution of thermal quenching to the observed decrease of the OH· concentration in the methane/1-butene flame is the ratio F_1/F_2.

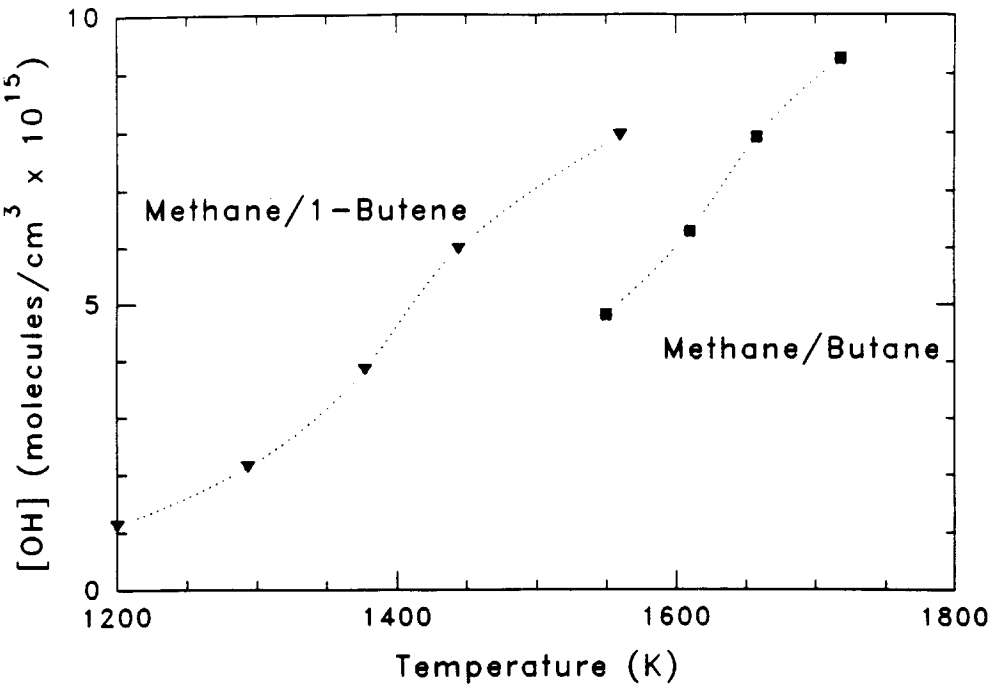

Fig. 7. The dependence of the OH · concentration on the temperature in the methane/butane and the methane/1-butene flames for $\phi \leq 0.85$ obtained at the location of the maximum OH · concentrations and in leaner flame regions.

Table 2 summarizes the values of F_1, F_2, F_1/F_2 for three temperature ratios T_1/T_2 at $\phi \leq 0.95$ in these two flames. Since a common temperature regime was not available for $\phi \leq 0.95$ along the centerline, a temperature ratio approach has been used. As this temperature ratio increases, both F_1 and F_2 increase. However, the ratio F_1/F_2 does not show any systematic change and is approximately 0.07, which indicates that the contribution of thermal quenching to the observed decrease of the centerline OH · concentration is only 7% in the methane/1-butene flame. In light of the uncertainty in establishing [OH ·] = $f(T)$, this value could be in error by ±50%. Nevertheless, this analysis indicates that the consumption of OH · by soot and/or CO is mainly responsible for the low OH · concentration in the central region of the methane/1-butene flame (see Fig. 4).

TABLE 2

Evaluation of the Relative Contribution of Thermal Quenching to the Observed Decrease in the OH · Concentration Along the Centerline of the Methane/1-Butene Flame[a]

T_1/T_2	F_1	F_2	F_1/F_2
1.19	1.86	22.9	0.08
1.22	2.25	24.2	0.09
1.28	3.72	93.6	0.04

[a] 1, methane/butane flame; 2, methane/1-butene flame.

C. Soot Oxidation Rates by OH · and O_2

An evaluation of the competition between soot and CO for oxidizing species requires knowledge of their individual oxidation rates, particularly due to OH · . The reaction rate for soot particles can be expressed in terms of the temporal evolution of the soot volume fraction:

$$R_{\text{Soot}} = \rho \frac{df_v}{dt}, \tag{5}$$

where ρ is the density of the soot particles. This rate can also be characterized from the time dependence of the $d_{p_{30}}$ profiles by substituting f_v from Eq. 1 into the above expression. Treating N_p as constant along a streamline

and assuming $\rho = 1.8$ g/cm^3 (150 kmol/m^3 for an atomic weight of 12) gives

$$R_{\text{Soot}} = 235.6 N_p d_{p_{30}}^2 \frac{d(d_{p_{30}})}{dt}, \quad (6)$$

where the units of R_{soot}, N_p, $d_{p_{30}}$, and $d(d_{p_{30}})/dt$ are kmol/m^3-s, cm^{-3}, cm, and cm/s, respectively. The assumption of a constant soot particle density is based upon the observation that no internal cavities are detected in soot particles collected from the oxidation region of diffusion flames [25]. Furthermore, there exist no experimental data to indicate a change in density of soot particles in this region.

The number concentration of primary particles, N_p, calculated from consistent f_v and $d_{p_{30}}$ measurements, is almost a factor of two lower in the methane flame (2.1×10^{11} cm^{-3}) than that in the methane/butane and the methane/1-butene flames (3.7×10^{11} cm^{-3}). The slope of the $d_{p_{30}}$ profile as a function of time is evaluated from a combination of second-, third-, and fourth-order polynomial fits. For the methane and methane/butane flames the fits also include the fact that the diameter of the primary particles must approach zero at the location of the visible flame tip (see Fig. 5). This procedure ensures a more accurate slope at the last temporal measurement locations. For the earliest time in the methane flame, however, the slope of the $d_{p_{30}}$ profile is quite uncertain since the primary particle size is expected to be close to its maximum value (see section III. B). Employing the fitting procedure just described in conjunction with Eq. 6 gives the net reaction rate (growth as well as oxidation) due to all species. Note that the use of d_p measurements in conjunction with Eq. 6 is a more direct way of determining the soot oxidation rate than Eq. 5 and the soot volume fraction measurements. The d_p results are preferred since the local soot volume fraction is obtained from tomographic inversion of laser light extinction data, which can result in significant uncertainties at the centerline.

The soot oxidation rate can be obtained from the temporal evolution of the $d_{p_{30}}$ profiles only at locations where soot growth species (i.e., hydrocarbons) are absent. In this region, which is typically fuel lean, the soot oxidation rate due to OH · can be determined by subtracting contributions due to other oxidizing species. For the conditions of this study the equilibrium O-atom concentration is calculated to be 2–3 orders of magnitude lower than the equilibrium OH · concentration. Therefore, the relative contribution of O atoms to the total soot oxidation rate is expected to be small, even though superequilibrium O-atom concentrations are likely [19] and the collision efficiency for the oxidation of soot by O atoms is high [34]. In the present analysis the only oxidizing species are assumed to be OH · and O_2.

Based upon these considerations, the soot oxidation rate due to OH · alone is given by:

$$\left.\frac{d[\text{Soot}]}{dt}\right|_{\text{OH}\cdot} = \left.\frac{d[\text{Soot}]}{dt}\right|_{\text{meas}} - \left.\frac{d[\text{Soot}]}{dt}\right|_{\text{O}_2}, \quad (7)$$

where the oxidation rate due to O_2 is estimated from the Nagle and Strickland-Constable (NSC) expression [3]. These OH · and O_2 contributions to the observed soot oxidation rate are presented in Fig. 8 and show that the contribution of O_2 to the observed soot oxidation rate is small throughout the oxidaton region in all three flames studied.

Use of the NSC expression to estimate the O_2 contribution to the soot oxidation rate is subject to some uncertainty. Numerous investigators [35–39] have compared experimental oxidation rates of various carbons with the NSC expression and report rates that range between a factor of 20 lower to a factor of 6 higher than that given by NSC values. However, the trend in the reported comparisons suggests that the NSC expression overpredicts the O_2 contribution to soot oxidation at lower temperatures and possibly underpredicts O_2 contributions at higher temperatures (see below). Of particular interest is recent work on the oxidation of soot [35] and synthetic chars [36] by O_2 that indicates the use of the NSC rate expression overestimates the O_2 oxidation rate at temperatures below 1800 K. Note that the centerline temperatures in the methane, methane/butane, and methane/butene flames range be-

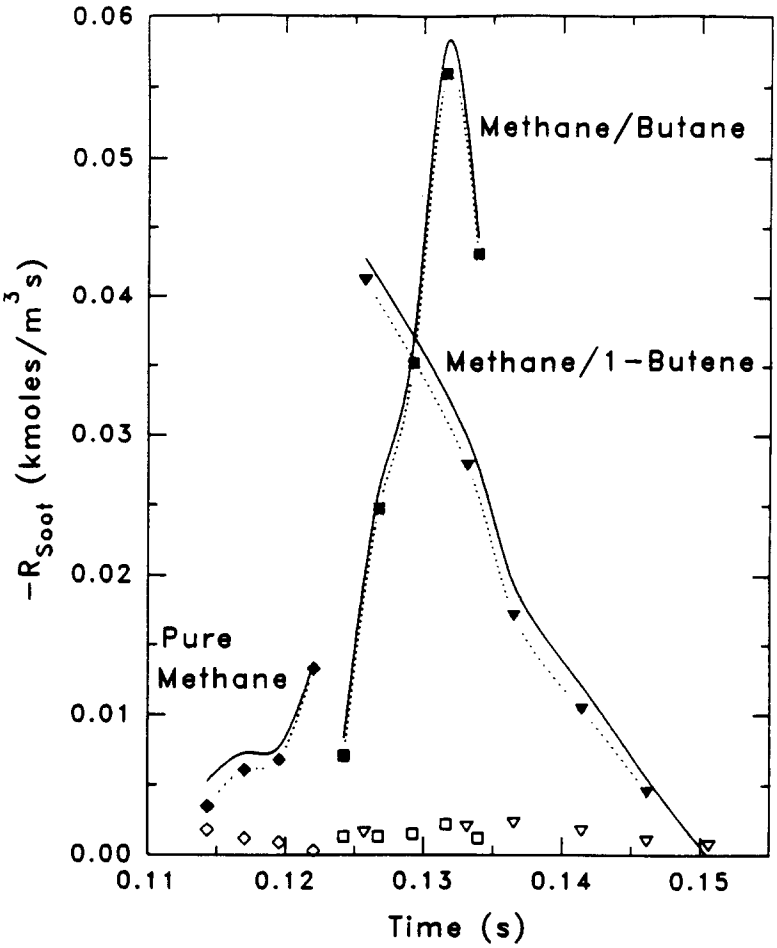

Fig. 8. Plots of the observed centerline soot oxidation rate, shown as a solid line. The contribution of O_2 as determined by the NSC expression (open symbols) and the derived soot oxidation rate due to OH · (from Eq. 7; solid symbols connected by dotted curve) are shown for the pure methane (◇, ◆), the methane/butane (□, ■) and the methane/1-butene (▽, ▼) flames.

tween 1610–1798 K, 1494–1660 K, and 1236–1469 K, respectively (see Table 1).

Chan et al. [35] studied the low-temperature oxidation of soot in a propane diffusion flame and the oxidation of collected soot in an O_2/N_2 environment using an isothermal thermogravimetric technique. The oxidation rate of soot in the thermogravimetric study was an order of magnitude lower than that predicted by the NSC rate for a temperature of ~ 1100 K. At the same temperature these workers [35] report good agreement wth the NSC rate for the diffusion flame study in which the soot oxidation rate was attributed completely to O_2 reactions. However, using an estimated equilibrium concentration of OH · for the conditions of their diffusion flame yields a soot oxidation rate (assuming a collision efficiency of 0.1 [4]) that is 3 times faster than the NSC rate. Thus, it is likely that OH · reactions were important in their propane diffusion flame and the soot oxidation rate due to O_2 was overestimated by Chan et al. [35].

The work of Levendis et al. [36] on synthetic chars reports good agreement with the NSC rate only at higher temperatures (1800–2300 K). These workers observed oxidation rates to be 20 times lower than the NSC rate in the temperature range 800–1600 K. They ascribed the increase in reactivity of the chars above

1600 K to graphitization, which increased the total surface area. Felder et al. [37] also find the NSC expression to overpredict the oxidation kinetics of carbon blacks in the 1300–1700 K temperature range. In the upper temperature regime (i.e., above the apparent graphitization temperature of 1600 K reported by Levendis et al. [36], Cadman et al. [38] report a factor of 6 higher soot oxidation rates compared with the NSC rate. In addition, Park and Appleton [39] justified the use of the NSC expression for soot oxidation based on shock tube experiments at higher temperatures (1700–4000 K).

In light of the studies cited above, the use of the NSC rate probably overestimates the soot oxidation rate due to O_2 in the oxidation region of the flames investigated here. This would give a larger contribution of OH · to the observed soot oxidation rate, but the increase would be slight since the O_2 contribution is already small (Fig. 8).

D. Collision Efficiencies of OH · with Soot Particles

The soot oxidation rate due to OH · is often discussed from a fundamental kinetic theory viewpoint, which incorporates a collision efficiency parameter. This parameter is defined as the fraction of collisions that result in a carbon atom being removed from soot. Thus, the collision efficiency η is simply a means of matching the observed soot oxidation rates with the following expression obtained by considering OH · to be an ideal gas colliding with a soot surface:

$$R_{\text{Soot}} = \eta\left(4.6 \times 10^{-18} d_p^2 N_p [\text{OH}\cdot]\sqrt{T}\right). \quad (8)$$

Here R_{soot} is expressed in kmol/m^3-s and the units of d_p, N_p, [OH ·], and T are cm, cm^{-3}, molecules/cm^3, and degrees Kelvin, respectively. Estimates of the collision efficiency can be obtained by equating Eqs. 7 and 8.

Table 3 summarizes the values of η determined in the three flames at the various measurement locations. The asterisks denote either regions where soot particle growth is taking place (for example, in the methane/butane flame) or regions where the estimated contribution due to O_2 is greater than the total soot reaction rate (in the methane/1-butene flame).

TABLE 3

Summary of the Collision Efficiency, η, Between Soot and OH · Obtained in the Three Flames as a Function of Time Along the Centerline Streamline[a]

Methane		Methane/Butane		Methane/1-Butene	
Time (s)	$\eta_{OH\cdot}$	Time (s)	$\eta_{OH\cdot}$	Time (s)	$\eta_{OH\cdot}$
0.114	0.120	0.119	*	0.126	0.65
0.117	0.043	0.122	*	0.131	0.37
0.120	0.030	0.124	0.044	0.137	0.13
0.122	0.050	0.127	0.065	0.141	0.10
—	—	0.129	0.070	0.146	0.18
—	—	0.132	0.079	0.151	*
—	—	0.134	0.140	—	—

[a] —, no measurements; *, η for OH · cannot be determined.

The first data point in the methane flame yields a higher value for η than at later times. As mentioned earlier (section III.B), here the value of $d_{p_{30}}$ should be close to its maximum along the centerline, and thus the net soot reaction rate should be close to zero. The other calculated values of η are roughly constant for the methane flame, with the average value being 0.04.

In the methane/butane flame the collision efficiency shows an increase with time. The average of all the determinations is 0.08. For the methane/1-butene flame the collision efficiencies are found to be the highest. However, the first two values are unrealistically large and are likely to be in error due to the uncertainty in collecting samples across the high soot volume fraction annular region (see section III.B). Omitting these two values, the average collision efficiency between OH · and soot is 0.14.

The collision efficiencies determined for these flames fall within the range of values reported in prior investigations. Neoh et al. [4] measured an average value of 0.13 based on the primary particle size. The data of Roth et al. [40] exhibit large scatter for η, ranging from 0.1 to more than 0.3. Note that in both of these studies the OH · concentration was not measured directly. Neoh et al. obtained the OH · concentration from a partial equilibrium estimate, and Roth et al. utilized the H_2/air mechanism given by Warnatz [41]. Mulcahy and Young [32] determined an effective upper limit of η for the gasification of carbon to be

0.08. These workers generated OH · by the following reaction:

$$H \cdot + NO_2 \rightarrow OH \cdot + NO$$

and obtained the OH · concentration by measuring the equimolar concentration of NO with a mass spectrometer.

The collision efficiency results described above reveal some interesting features. Not only do the derived collision efficiencies generally increase with time as soot oxidation proceeds, they also are larger in the flames with more soot. Figure 9 presents a striking correlation of the selected values of η with residence time; the collision efficiency increases at a rate of $4.8 \pm 0.8 \times 10^{-3}$/ms. This result suggests that either (a) the soot particle reactivity changes with time, and/or (b) other oxidizing species are important. The inclusion of additional species in Eq. 7 would reduce both the soot oxidation rate due to OH · and its collision efficiency η.

The soot particle reactivity is known to change in the growth region of hydrocarbon flames [42–44]. This observation has been interpreted in terms of the concept of active sites. The growth of soot particles is argued [11] to accelerate after the inception region due to collisions of reactive species with the particle surface which produce active sites. At later times the reactivity of the soot particles changes due to thermal annealing or radical site stabilization processes [12, 13]. The modeling results of Frenklach and Wang [45] indicate that the fraction of surface sites available for reaction (α) is lower at higher temperatures. They conclude that α is determined by steric effects, with the mobile soot particle crystallites aligning themselves to limit access to gaseous species at higher temperatures. The collision efficiencies determined here are plotted as a function of temperature in Fig. 10 and reveal a slow decrease at a rate of $-2.2 \pm 0.6 \times 10^{-2}$/100 K. In terms of active sites, the collision efficiency should reflect the fraction of surface sites that are active (α). The variation of η with temperature shown in Fig. 10 is consistent with fewer active sites being present at higher temperatures.

A second possible explanation for the apparent change in soot particle reactivity involves the presence of oxidizing species other than O_2 and OH · considered here. Dixon-Lewis et al. [5] have proposed a mechanism in which radicals catalyze attack by molecular oxygen. In their scheme the OH · radicals or O atoms,

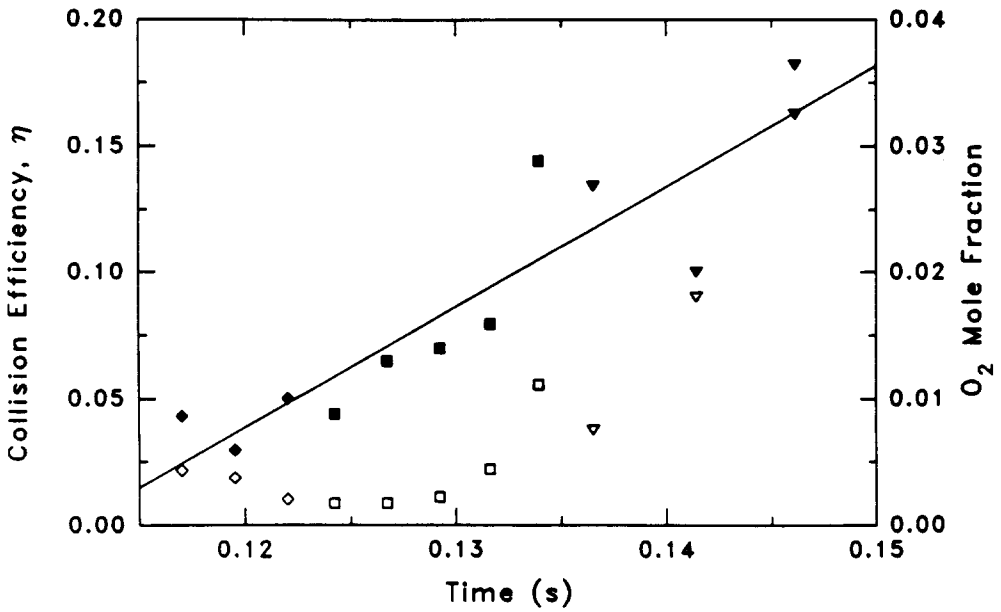

Fig. 9. Plots of the collision efficiency, η (solid symbols), and the O_2 mole fraction (open symbols) as a function of residence time along the centerline of the methane (◇, ◆), methane/butane (□, ■), and methane/1-butene flames (▽, ▼). The line is a linear least squares fit to the collision efficiency data.

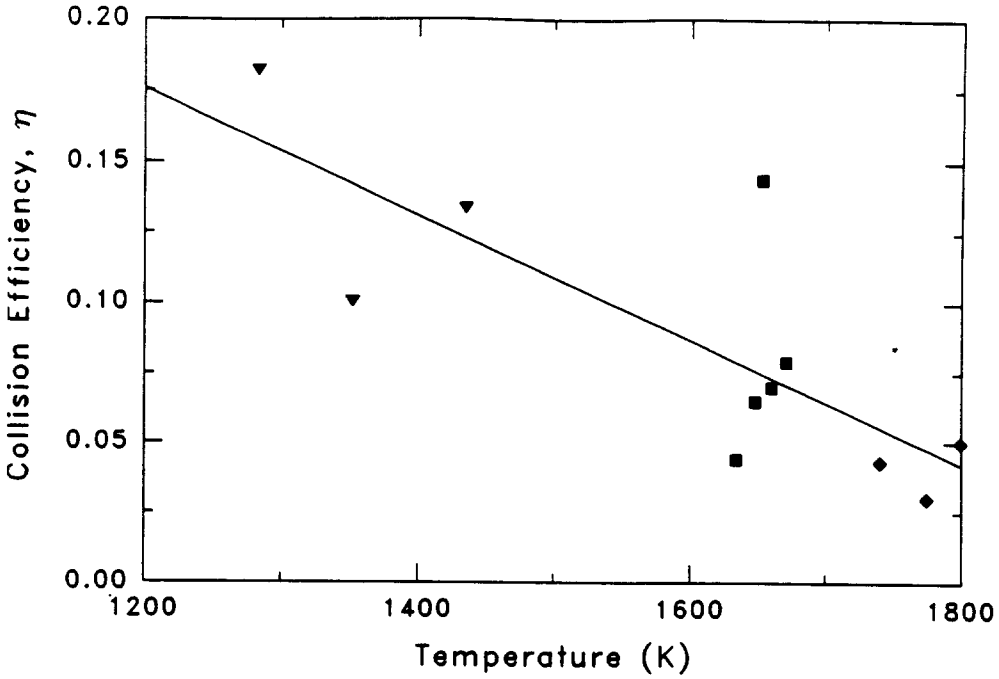

Fig. 10. Plot of the collision efficiency, η, estimated from the soot oxidation rates and the OH · concentrations as a function of temperature in the methane (◆), methane/butane (■), and methane/1-butene (▼) flames. The line is a linear least squares fit to the data.

formed from the reaction of molecular O_2 with H atoms, attack carbon more effectively than O_2. This explains the observed increased oxidation rate of graphite introduced into the main reaction zone of premixed flames. Figure 9 includes O_2 concentration data along with the calculated values of η as a function of time. The O_2 concentrations do not change substantially at early times (and at the higher temperatures). The H-atom concentration is expected to exhibit a maximum value near $\phi = 1.0$ [19]. Thus, the H-atom concentration should be decreasing for the last two points in the methane/butane flame and the three points in the methane/1-butene flame (see Table 1). Although the data for the methane/1-butene flame show larger O_2 concentrations, the temperatures are much lower and so is the expected H-atom concentration. Thus, the catalytic mechanism does not account for the observed increased reactivity over the whole range of our experimental conditions.

In summary, the observed increase in the collision efficiency of soot oxidation by OH · with time most likely arises from an increasing reactivity of the soot particles. It is interesting to note that the flames that form more soot (possibly due to a larger fraction of active sites, α) also exhibit larger collision efficiencies with OH · . At this point one cannot determine whether the increased reactivity is a result of (1) the lower temperatures in more highly sooting flames and hence an increase fraction of surface sites available for reaction due to greater access to gaseous species, as proposed by Frenklach and Wang [45], or (2) the fact that a greater number of active sites, which originate in the inception zone and produce a larger soot concentration, are still available in the soot oxidation region and are involved in oxidation reactions.

E. Competition for OH · between CO and Soot

The competition between CO and soot for OH · can be evaluated by comparing the soot oxidation rate computed from Eq. 8 with the forward rate of the CO + OH · reaction [46]:

$$\frac{d[\mathrm{CO}]}{dt} = 1.5 \times 10^4 T^{1.3} e^{386/T}[\mathrm{CO}][\mathrm{OH}\cdot], \quad (9)$$

where $d[CO]/dt$ is given in kmol/m^3-s. The collision efficiency values for this analysis have been obtained from the linear least squares fit shown in Fig. 9. Since both the CO and soot oxidation rates have a first-order dependence on their respective concentrations, it is also appropriate to compare their normalized rates. If we consider

$$F_3 = \frac{\dfrac{d[CO]}{dt}}{\dfrac{d[Soot]}{dt}} \quad \text{and}$$

$$F_4 = \frac{\dfrac{1}{[CO]} \times \dfrac{d[CO]}{dt}}{\dfrac{1}{[Soot]} \times \dfrac{d[Soot]}{dt}}, \tag{10}$$

then the ratio F_3 is an indication of the amount of competition between CO and soot for OH $\cdot$. For example, a value of $F_3 = 1$ implies an equal probability that an OH $\cdot$ molecule will react with CO or soot. The ratio F_4 reflects the intrinsic reactivity of OH $\cdot$ with CO vs. soot and is a function of the collision efficiency η, the primary particle size $d_{p_{30}}$, and the temperature T (see Eqs. 1, 8, and 9):

$$F_4 \propto \frac{d_p T^{0.8} e^{386/T}}{\eta}. \tag{11}$$

The direct dependence of F_4 on the primary particle size is intuitively understandable, since for the same soot volume fraction a larger d_p will result in a smaller soot oxidation rate due to the decreased surface area. With increasing temperature the ratio F_4 increases due to a higher inherent reactivity of CO and a lower inherent reactivity of soot (smaller η).

Table 4 summarizes the ratios F_3 and F_4 determined for the three flames at various values of the residence time. The methane flame shows the least competition between CO and soot for OH $\cdot$, as reflected by the high values for F_3 and F_4. The OH $\cdot$ + CO rate is far larger than that for OH $\cdot$ + soot. This is due both to a low soot reactivity (Table 3) and to the low soot concentration. As the soot concentration increases in the methane/butane and methane/1-butene flames, the competition between CO and soot for OH $\cdot$ increases. In the methane/1-butene flame, the soot oxidizes faster than CO at all but the two earliest residence times shown in Table 4. With increasing time in all of the flames, an increasing value of η increases the OH $\cdot$ + soot oxidation rate relative to the OH $\cdot$ + CO rate. This is reflected by the decreasing values of F_4 with time. Although CO is intrinsically more reactive with OH $\cdot$ than with soot in all of the flames of this study (i.e., the F_4 values are all greater than 1), its oxidation is suppressed in the presence of large soot concentrations. This is most evident in the methane/1-butene flame.

V. CONCLUSIONS

Measurements of the hydroxyl radical concentration and the size of the primary soot particles have been made in a series of hydrocarbon/air diffusion flames containing varying

TABLE 4

Summary of the Ratio of the CO Oxidation Rate to the Soot Oxidation Rate (F_3) and the Ratio of the Normalized CO Reaction Rate to the Normalized Soot Oxidation Rate (F_4) in the Three Flames

Methane			Methane/Butane			Methane/1-Butene		
Time (s)	F_3	F_4	Time (s)	F_3	F_4	Time (s)	F_3	F_4
0.114	82.7	25.3	0.119	13.6	12.2	0.126	2.31	10.0
0.117	42.6	13.1	0.122	6.3	10.3	0.131	1.13	7.1
0.120	21.9	8.9	0.124	3.7	8.0	0.137	0.47	5.2
0.122	12.3	5.9	0.127	1.9	6.7	0.141	0.23	4.2
—	—	—	0.129	1.1	5.3	0.146	0.13	3.4
—	—	—	0.132	0.9	4.1	0.151	0.07	3.0
—	—	—	0.134	0.9	2.0	—	—	—

amounts of soot. The observed OH · concentrations are suppressed in the presence of soot particles. A comparison of the fuel lean OH · concentrations in the presence and absence of soot particles reveals that the OH · concentraton is reduced primarily due to reactions with soot rather than as a consequence of the lower flame temperatures measured for the higher soot loadings. The effect of lower temperatures on the OH · concentration is comparatively small, accounting for only 7% ± 4% of the measured decrease in the OH · concentration.

The soot oxidation rates computed from the primary particle size profiles as a function of time reveal interesting trends for the soot particle reactivity. Higher collision efficiencies are deduced for the flames containing larger soot concentrations at lower temperatures. The variation of the collision efficiency with temperature suggests that fewer active sites per unit surface area exist at higher temperatures.

A comparison of the soot and CO oxidation rates shows that although CO is inherently more reactive than soot on a per carbon basis, for large soot concentrations the soot successfully competes with CO for OH · and hence suppresses CO oxidation. The soot oxidation rates due to OH · were obtained by subtracting the contribution due to O_2 (determined from the Nagle Strickland-Constable expression [3]) from the observed rates. Although the NSC expression is likely to overestimate the soot oxidation rate due to O_2 under the conditions of this study, the contribution of O_2 to the soot oxidation rate is found to be small compared with that due to OH · .

The work done at the Pennsylvania State University was supported under grant 60NANB0D1035 from the National Institute of Standards and Technology. The assistance of Marlow Moser with the instrumentation is gratefully acknowledged.

REFERENCES

1. Puri, R., and Santoro, R. J., *Fire Safety Science—Proceedings of the Third International Symposium*, 1991, pp. 595–604.
2. Fenimore, C. P., and Jones, G. W., *J. Phys. Chem.* 71:593–597 (1967).
3. Nagle, J., and Strickland-Constable, R. F., *Proceedings of the Fifth Carbon Conference*, Pergamon, Oxford, 1962, Vol. 1, pp. 154–164.
4. Neoh, K. G., Howard, J. B., and Sarofim, A. F., *Particulate Carbon Formation During Combustion*, (D. C. Siegla and G. W. Smith, Eds.), Plenum, New York, 1981, pp. 261–282.
5. Dixon-Lewis, G., Bradley, D., and El-Din Habik, S., *Combust. Flame* 86:12–20 (1991).
6. Garo, A., Prado, G., and Lahaye, J., *Combust. Flame* 79:226–233 (1990).
7. Dobbins, R. A., and Megaridis, C. M., *Langmuir* 3:254–259 (1987).
8. Dobbins, R. A., Santoro, R. J., and Semerjian, H. G., *Twenty-Third Symposium (International) on Combustion*, The Combustion Institute, Pittsburgh, 1990, p. 1525.
9. Walker, P. L. Jr., Rusinko, F. Jr., and Austin, L. G., *Adv. Catal.* 11:133–221 (1959).
10. Howard, J. B., *Twenty-Third Symposium (International) on Combustion*, The Combustion Institute, Pittsburgh, 1990, p. 1107.
11. Tesner, P. A., *Combust. Flame* 86:187–188 (1991).
12. Woods, I. T., and Haynes, B. S., *Combust. Flame* 85:523–525 (1991).
13. Harris, S. J., *Combust. Sci. Technol.* 72:67–77 (1990).
14. Saito, K., Gordon, A. S., Williams, F. A., and Stickle, W. F., *Combust. Sci. Technol.* 80:103–119 (1991).
15. Toossi, R., *Combust. Flame* 90:1–10 (1992).
16. Puri, R., Moser, M., Santoro, R. J., and Smyth, K. C., *Twenty-Fourth Symposium (International) on Combustion*, The Combustion Institute, Pittsburgh, 1992, p. 1015.
17. Santoro, R. J., Semerjian, H. G., and Dobbins, R. A., *Combust. Flame* 51:203–218 (1983).
18. Smyth, K. C., Miller, J. H., Dorfman, R. C., Mallard, W. G., and Santoro, R. J., *Combust. Flame* 62:157–181 (1985).
19. Smyth, K. C., Tjossem, P. J. H., Hamins, A., and Miller, J. H., *Combust. Flame* 79:366–380 (1990).
20. Fairchild, P. W., Smith, G. P., and Crosley, D. R., *J. Chem. Phys.* 79:1795–1807 (1983).
21. Smith, G. P., and Crosley, D. R., *J. Chem. Phys.* 85:3896–3901 (1986).
22. Richardson, T. F., Ph.D. dissertation, Department of Mechanical Engineering, The Pennsylvania State University, 1993.
23. Puri, R., Richardson, T. F., Santoro, R. J., and Dobbins, R. A., *Combust. Flame* 92:320–333 (1993).
24. Prado, G., Jagoda, J., Neoh, K., and Lahaye, J., *Eighteenth Symposium (International) on Combustion*, The Combustion Institute, Pittsburgh, 1981, p. 1127.
25. Megaridis, C. M., and Dobbins, R. A., *Combust. Sci. Technol.* 66:1–16 (1989).
26. Köylü, Ü. Ö., Sivathanu, Y. R., and Faeth, G. M., *Fire Safety Science—Proceedings of the Third International Symposium*, 1991, pp. 625–634.
27. Gordon, S., and McBride, B. J., NASA SP-273 Interim Revision N78-17724, March 1976.
28. Kennedy, I. M., Kollmann, W., and Chen, J.-Y., *Combust. Flame* 81:73–85 (1990).

29. Kennedy, I. M., Kollmann, W., and Chen, J.-Y., *AIAA J.* 29:1452–1457 (1991).
30. Moss, J. B., Stewart, C. D., and Syed, K. J., *Twenty-Second Symposium (International) on Combustion*, The Combustion Institute, Pittsburgh, 1988, p. 413.
31. Leung, K. M., Lindstedt, R. P., and Jones, W. P., *Combust. Flame* 87:289–305 (1991).
32. Mulcahy, M. F. R., and Young, B. C., *Carbon* 13:115–124 (1975).
33. Baulch, D. L., Cobos, C. J., Cox, R. A., Esser, C., Frank, P., Just, Th., Kerr, J. A., Pilling, M. J., Troe, J., Walker, R. W., and Warnatz, J., *J. Phys. Chem. Ref. Data* 21:411–734 (1992).
34. Gersum, S. von, and Roth, P. *Twenty-Fourth Symposium (International) on Combustion*, The Combustion Institute, Pittsburgh, 1992, p. 999.
35. Chan, M.-L., Moody, K. N., Mullins, J. R., and Williams, A., *Fuel* 66:1694–1698 (1987).
36. Levendis, Y. A., Flagan, R. C., and Gavalas, G. R., *Combust. Flame* 76:221–241 (1989).
37. Felder, W., Madronich, S., and Olson, D. B., *Ener. Fuels* 2:743–750 (1988).
38. Cadman, P., Cornish, R., and Denning, R. J., *Seventeenth International Shock Tube Symposium*, 1990, pp. 751–755.
39. Park, C., and Appleton, J. P., *Combust. Flame* 20:369–379 (1973).
40. Roth, P., Brandt, O., and Gersum, S. von, *Twenty-Third Symposium (International) on Combustion*, The Combustion Institute, Pittsburgh, 1990, p. 1485.
41. Warnatz, J., *Ber. Bunsenges. Phys. Chem.* 87:1008–1022 (1983).
42. Harris, S. J., and Weiner, A. M., *Combust. Sci. Technol.* 31:155–167 (1983); 32:267–275 (1983); 38:75–87 (1984).
43. Bockhorn, H., Fetting, F., Heddrich, A., and Wannemacher, G., *Twentieth Symposium (International) on Combustion*, The Combustion Institute, Pittsburgh, 1984, p. 979.
44. Baumgärtner, L., Hesse, D., Jander, H., and Wagner, H. Gg., *Twentieth Symposium (International) on Combustion*, The Combustion Institute, Pittsburgh, 1984, p. 959.
45. Frenklach, M., and Wang, H., *Twenty-Third Symposium (International) on Combustion*, The Combustion Institute, Pittsburgh, 1990, p. 1559.
46. Wilk, R. D., Cernansky, N. P., Pitz, W. J., and Westbrook, C. K., *Combust. Flame* 77:145–170 (1989).

Received 12 March 1993; revised 17 September 1993